Antarctic ice sheet sensitivity to atmospheric CO_2 variations in the early to mid-Miocene

Richard Levy[a,1], David Harwood[b], Fabio Florindo[c], Francesca Sangiorgi[d], Robert Tripati[e,f], Hilmar von Eynatten[g], Edward Gasson[h], Gerhard Kuhn[i], Aradhna Tripati[e,f], Robert DeConto[h], Christopher Fielding[b], Brad Field[a], Nicholas Golledge[a,j], Robert McKay[j], Timothy Naish[a,j], Matthew Olney[k], David Pollard[l], Stefan Schouten[m], Franco Talarico[n], Sophie Warny[o], Veronica Willmott[i], Gary Acton[p], Kurt Panter[q], Timothy Paulsen[r], Marco Taviani[s], and SMS Science Team[2]

[a]Department of Paleontology, GNS Science, Lower Hutt, New Zealand, 5040; [b]Department of Earth & Atmospheric Sciences, University of Nebraska, Lincoln, NE 68588; [c]Istituto Nazionale di Geofisica e Vulcanologia, I-00143 Rome, Italy; [d]Marine Palynology and Paleoceanography, Laboratory of Palaeobotany and Palynology, Department of Earth Sciences, Utrecht University, 3584 CD, Utrecht, The Netherlands; [e]Institute of the Environment and Sustainability, University of California, Los Angeles, CA 90024; [f]Department of Atmospheric and Oceanic Sciences, University of California, Los Angeles, CA 90095; [g]Department of Sedimentology & Environmental Geology, Geoscience Center Göttingen, 37077 Göttingen, Germany; [h]Department of Geosciences, University of Massachusetts, Amherst, MA 01003; [i]Alfred Wegener Institute for Polar & Marine Research, 27568 Bremerhaven, Germany; [j]Antarctic Research Centre, Victoria University of Wellington, Wellington, New Zealand, 6012; [k]Hillsborough Community College, Tampa, FL 10414; [l]Earth & Environmental Systems Institute, Pennsylvania State University, University Park, PA 16802; [m]Marine Organic Biogeochemistry, Royal Netherlands Institute for Sea Research, 1797 SZ 't Horntje (Texel), The Netherlands; [n]Dipartimento di Scienze Fisiche della Terra e dell'Ambiente, Università degli Studi di Siena, I-53100 Siena, Italy; [o]Department of Geology & Geophysics and Museum of Natural Science, Louisiana State University, Baton Rouge, LA 70803; [p]Department of Geography & Geology, Sam Houston State University, Huntsville, TX 77341; [q]Department of Geology, Bowling Green State University, Bowling Green, OH 43403; [r]Department of Geology, University of Wisconsin-Oshkosh, Oshkosh, WI 54901; and [s]Institute of Marine Sciences, National Research Council, 40129 Bologna, Italy

Geological records from the Antarctic margin offer direct evidence of environmental variability at high southern latitudes and provide insight regarding ice sheet sensitivity to past climate change. The early to mid-Miocene (23–14 Mya) is a compelling interval to study as global temperatures and atmospheric CO_2 concentrations were similar to those projected for coming centuries. Importantly, this time interval includes the Miocene Climatic Optimum, a period of global warmth during which average surface temperatures were 3–4 °C higher than today. Miocene sediments in the ANDRILL-2A drill core from the Western Ross Sea, Antarctica, indicate that the Antarctic ice sheet (AIS) was highly variable through this key time interval. A multiproxy dataset derived from the core identifies four distinct environmental motifs based on changes in sedimentary facies, fossil assemblages, geochemistry, and paleotemperature. Four major disconformities in the drill core coincide with regional seismic discontinuities and reflect transient expansion of grounded ice across the Ross Sea. They correlate with major positive shifts in benthic oxygen isotope records and generally coincide with intervals when atmospheric CO_2 concentrations were at or below preindustrial levels (~280 ppm). Five intervals reflect ice sheet minima and air temperatures warm enough for substantial ice mass loss during episodes of high (~500 ppm) atmospheric CO_2. These new drill core data and associated ice sheet modeling experiments indicate that polar climate and the AIS were highly sensitive to relatively small changes in atmospheric CO_2 during the early to mid-Miocene.

Antarctica | ice sheet | Climate Optimum | Ross Sea | Miocene

Knowledge regarding Antarctic ice sheet (AIS) response to warming climate is of fundamental importance due to the role ice sheets play in global sea level change. Paleoenvironmental records from Earth's past offer a means to examine AIS variability under climatic conditions that were similar to today and those projected for the next several decades (1, 2). In this respect, the early to mid-Miocene is a compelling interval to study as proxy reconstructions of atmospheric CO_2, albeit uncertain, suggest that concentrations generally varied between preindustrial levels (PAL = 280 ppm) and values at or above 500 ppm (3–9). Additionally, global mean surface temperature during peak Miocene warmth was up to 3–4° higher than today (10), similar to best-estimate temperatures expected by 2100 under the highest projected greenhouse gas concentration pathway (Representative Concentration Pathway 8.5) (1, 2). Finally, Miocene geography was similar to today (11), and major circum-Antarctic oceanic and atmospheric circulation patterns that dominate the modern Southern Ocean were well established (12, 13).

Much of our understanding regarding AIS history through the early to mid-Miocene comes from far-field records from deep ocean basins. Benthic oxygen and carbon isotope proxies for global paleoclimate suggest that early to mid-Miocene climate and glacial environments were highly variable (14–19). These records include evidence for major transient glacial episodes and sea level fall, intervals of relative ice sheet stability, and periods of climatic warmth with major ice sheet retreat and sea level rise. Furthermore, reconstructions from sedimentary sequences on the Marion Plateau, offshore northeast Australia (20), and New Jersey margin (21) suggest sea level varied by up to 100 m. Episodes of sea level maxima (+40 m) suggest loss of Antarctica's marine-based ice sheets that, at present, occupy much of West Antarctica and large portions of East Antarctica (22), as well as substantial loss of mass from Antarctica's terrestrial ice sheets.

Significance

New information from the ANDRILL-2A drill core and a complementary ice sheet modeling study show that polar climate and Antarctic ice sheet (AIS) margins were highly dynamic during the early to mid-Miocene. Changes in extent of the AIS inferred by these studies suggest that high southern latitudes were sensitive to relatively small changes in atmospheric CO_2 (between 280 and 500 ppm). Importantly, reconstructions through intervals of peak warmth indicate that the AIS retreated beyond its terrestrial margin under atmospheric CO_2 conditions that were similar to those projected for the coming centuries.

EARTH, ATMOSPHERIC, AND PLANETARY SCIENCES

Episodes of maximum sea level fall (up to −60 m) suggest that the AIS occasionally grew and advanced across continental shelves.

Geological records proximal to Antarctica's coastal margin provide direct evidence of past ice sheet variability in response to changing global climate. The ANDRILL (AND)-2A drill core, a 1,138-m-long stratigraphic archive of climate and ice sheet variability from the McMurdo Sound sector of the western Ross Sea (77°45.488′S, 165°16.613′E), was recovered by drilling from an ~8.5-m-thick floating sea ice platform in 380 m of water, located ~30 km off the coast of Southern Victoria Land (SVL) (Fig. 1A) (23). The drill core comprises lower Miocene to Quaternary glacial-marine strata deposited in the steadily subsiding Victoria Land Basin (VLB) (24). Paleogeography was broadly similar to today, although continental shelves in the Ross and Weddell seas were likely shallower (*SI Text* and Fig. S1). Recovered core sediments, and the proxies they contain, allow us to assess past ice sheet dynamics along a coastal margin influenced by ice flowing from East Antarctica and across the West Antarctic continental shelf. Through analysis of an integrated proxy environmental dataset, we derive a new environmental reconstruction and combine this with a suite of global environmental data to establish a history of AIS response to global climate events and episodes during the early to mid-Miocene. This integrated dataset allows us to evaluate key drivers of high latitude climate and ice sheet variability between 21 and 13 Ma. Outcomes from research reported here and in a companion ice sheet modeling study (25) suggest the AIS advanced across continental shelves during cold orbital configurations and retreated well inland of the coast under warm orbits. This large range of AIS variability occurred under a relatively low range in atmospheric CO_2 concentration (~280–500 ppm) and indicates the Antarctic environment was highly sensitive during the early to mid-Miocene.

Results

A near-continuous record spanning 20.2 to ~14.4 Ma is preserved in the lower 925 m of AND-2A (Fig. 1B, Figs. S2 and S3, and Table S1). A diverse range of geological information including physical properties and sedimentological, paleontological, and geochemical data were collected (summarized in *SI Text*, Table S2, and refs. 23 and 26–33). Here we present new data including sea surface water (upper 200 m) temperatures (SWTs) derived from archaeal lipids (TEX^L_{86}) (Fig. S4 and Table S3) and carbonate isotopes (Δ_{47}) (Table S4), whole rock inorganic geochemical data, and an integrated age model (Fig. S2 and Table S2), and offer the first analysis, to our knowledge, of a combined proxy environmental dataset derived from AND-2A (Fig. 1B and Fig. S3). These paleoenvironmental data are used to define four characteristic environmental motifs (EMs) (Table S2) that reflect distinct climatic and glacial regimes (Fig. 1 A and B).

Intervals of maximum ice sheet extent and cold polar conditions are assigned to EM I (maximum ice) and are characterized in AND-2A by four major disconformities. These disconformities are relatively rare and represent distinct and discrete times of major ice sheet advance beyond the drill site onto the continental shelf (Fig. 1 C, i). Three disconformities AND2A-U1 [965.43 m below sea floor (mbsf)]; -U2 (774.94 mbsf); and -U3 (262.57 mbsf) span the time intervals ~20–19.8, ~18.7–17.8, and ~15.8–14.6 Ma, respectively (Fig. S2). A fourth major disconformity AND2A-U4 (214.13 mbsf) separates middle Miocene rocks (>~14.4 Ma; Fig. S2) from 214 m of overlying upper Miocene to Quaternary strata.
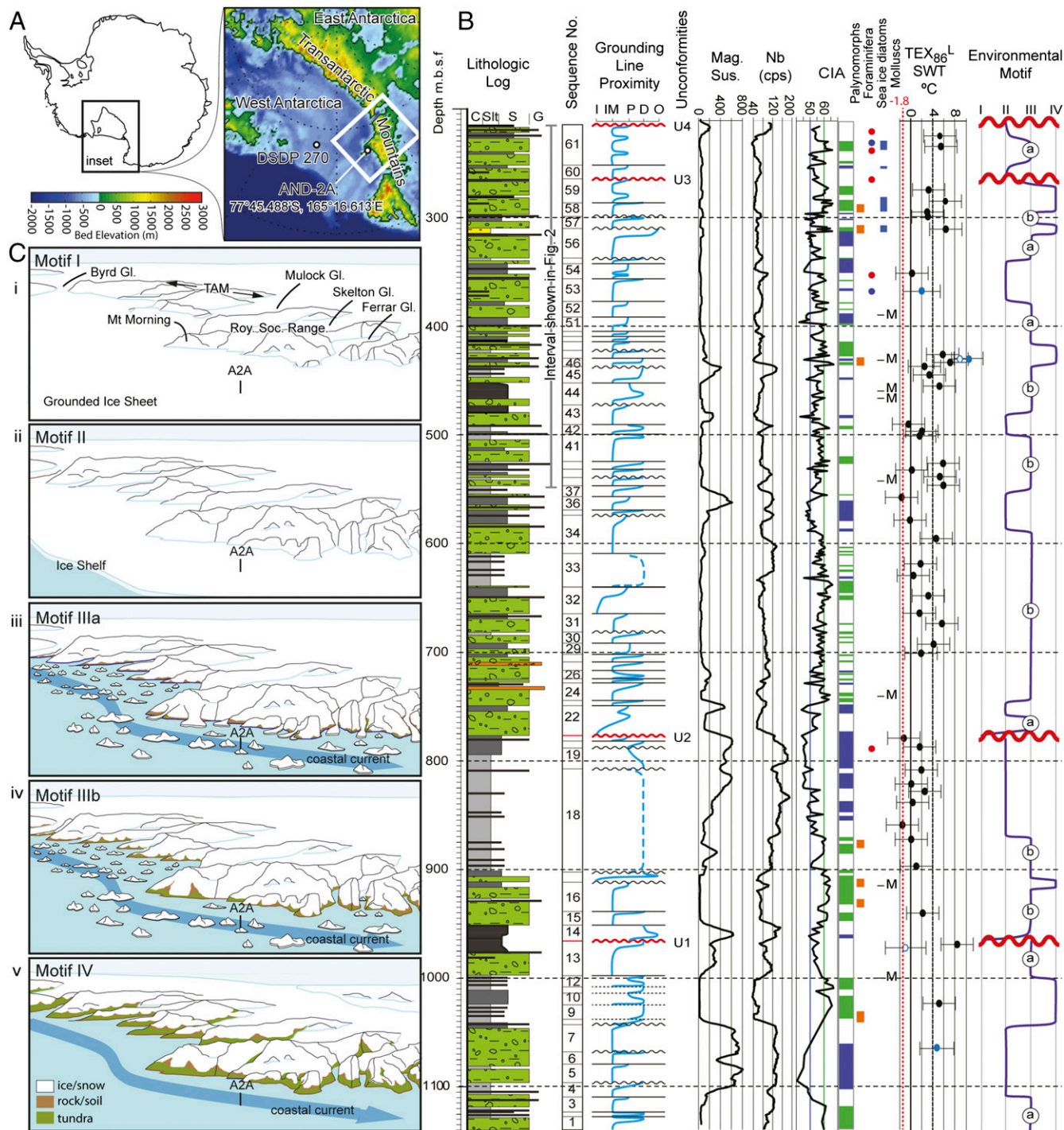
Eight stratigraphic intervals in AND-2A are assigned to EM II (cold polar), as characterized by high magnetic susceptibility (MS), high Niobium (Nb) content, and low chemical index of alteration (CIA), all of which reflect sediment derived from local volcanic centers and unweathered outcrop in proximal regions of the Transantarctic Mountains (TAM). We infer that relative increases in local sediment are due to advance of ice from expanding ice caps on nearby Mount Morning and the Royal Society Range under a cold polar climate. Five of the eight intervals are dominated

by massive to stratified diamictite facies that often contain debris derived from local volcanic sources and were probably deposited beneath a floating ice tongue or ice shelf proximal to the grounding line of outlet or piedmont glaciers (Fig. 1 C, ii). Each of these intervals is typically fossil poor. TEX^L_{86}-derived SWTs range between −1.4 and 2.6 ± 2.8 °C and are supported by a Δ_{47}-derived value of 2.1 ± 3.7 °C at 366 mbsf. We infer that proxies in EM II reflect cold polar conditions with minimum grounding-line variability and persistent floating ice shelves and/or coastal fast ice.

Twelve stratigraphic intervals are assigned to EM III (cold temperate) as characterized by low to moderate MS, low to moderate Nb content, and moderate to high CIA. These data indicate variable sediment provenance and periodic input from local volcanic sources and/or unweathered outcrop. EM III is divided into subtypes a and b based on variations in lithofacies and fossil content. EM IIIa is dominated by stratified diamictite and gravel with variable clast composition but including a high proportion of rock fragments sourced from the region south of Skelton and Mulock glaciers. Foraminifera vary in abundance and are absent in many intervals but include up to 10 species in others (30). Marine diatoms and terrestrial palynomorphs are usually absent but occur in low abundance in several discrete intervals. Mollusc-bearing intervals are uncommon. TEX^L_{86}-derived SWTs range between 2.2 and 5.4 ± 2.8 °C. Intervals characterized by EM IIIa likely reflect a subpolar climate and glacial regime with tidewater glaciers. Periodic increase in gravel clasts derived from regions south of Mount Morning reflect an increase in ice flux through major East Antarctic ice sheet (EAIS) outlet valleys into fjords under warmer conditions. During these intervals, calving rates at the grounding-line increased and debris-laden icebergs delivered sediment to the drill site as they drifted northwards along the SVL coast (Fig. 1 C, iii).

EM IIIb has persistently low Nb and MS, reflecting minimal input from local volcanic sources. Lithofacies are diverse and include massive and stratified diamictite and gravel; clast composition is mixed, with a high proportion of lithologies derived from the Skelton and Mulock glaciers and as far south as the Carlyon and Byrd glaciers. Intervals of mudrock dominated sequences are more common in EM IIIb than in EM IIIa. Terrestrial palynomorphs are more abundant in several intervals of EMIIIb (e.g., 947.54, 922.61, and 593.29 mbsf), and discrete intervals bearing mollusc fossils occur occasionally (Fig. 1B and Fig. S3). TEX^L_{86}-derived SWTs range from 0.2 to 6.7 ± 2.8 °C. We infer that EM IIIb reflects a depositional setting similar to EM IIIa but with a generally warmer climate, particularly during periods when SWTs were 6–7 ± 2.8 °C and local ice cap margins retreated to the coast and had limited influence on marine sedimentation at the drill site. Coarse clastic sediment was primarily delivered to the drill site by debris-rich icebergs derived from large fast flowing outlet glaciers to the south. Increased abundance of *Podocarpites* spp. and *Nothofagidites* spp. pollen (Fig. 1B and Fig. S3) indicates local tundra occupied ice-free regions along the coastal margin (Fig. 1 C, iv).

Five relatively short, lithologically diverse, stratigraphic intervals are assigned to EM IV (minimum ice) as characterized by low MS, low Nb content, and high CIA, which indicate minimal sediment input from local volcanic sources and/or unweathered outcrop. Lithofacies are variable, but sequences are usually dominated by mudrock, sandstone, and thin diamictite. A 46-m-thick section between 996.69 and 1,042.55 mbsf incorporates five sequences dominated by sediments deposited within a marine-deltaic setting distal to the glacial margin (27). The interval between 428.28 and 436.18 mbsf incorporates a single sequence comprising a basal diamictite overlain by a sandstone unit with relatively abundant marine bivalves. Thick-shelled costate scallops and venerid clams recovered from this interval indicate that water temperatures were at least 5 °C warmer than in the Ross Sea today (29). Relatively warm water temperatures are

Fig. 1. (A) Map showing Ross Sea area (*Inset*) and AND-2A drill site (white box indicates approximate area for schematic reconstructions shown below). (B) Stratigraphic summary of lower 925 m of AND-2A (214.13–1,138.54 mbsf) showing 61 sedimentary cycles. Glacial proximity curve tracks relative position of the grounding line through ice-contact (I), ice-marginal (IM), ice-proximal (P), ice-distal (D), and open marine (O) environments. Continuously acquired datasets include magnetic susceptibility and Niobium (Nb) XRF-CS counts. CIA (curve and bar) indicates arid (<50, blue) and less arid (>60, green) conditions. Intervals of peak palynomorph concentration shown by orange boxes. Foraminifera assemblages include cold water/ice marginal benthic species (red circles) and cool water planktonic species (blue circles). Blue bars, sea ice diatoms; M, intervals with well-preserved molluscs. Sea water temperature estimates based on TEX_{86}^L (black circles) and Δ_{47} (blue circles, open, less well-preserved specimens). Environmental Motif curve based on the proxy environmental dataset. (C) Schematic reconstructions of region around AND-2A showing likely conditions for each environmental motif (I–IV).

supported by TEX_{86}^L and Δ_{47} data, which indicate SWT at the coastal margin reached a maximum between 7.0 ± 2.8 °C and 10.4 ± 2.5 °C. In situ pollen and spores are abundant in this interval and indicate a coastal vegetation of mossy tundra with shrub podocarps and southern beech and suggest a cool terrestrial climate (10 °C January mean air temperature) (31–33). Evidence for another interval of warm climate is also preserved in a unique diatom-rich unit at ∼310 mbsf. This unit contains a typical tundra pollen assemblage recovered from other EM IV units but also includes freshwater algae and cosmopolitan dinoflagellate taxa

that indicate much warmer temperatures than occur in the Ross Sea today (32). Furthermore, TEX_{86}^L analyses from the diatomite unit indicate maximum surface water temperatures of ~6–7 ± 2.8 °C, which is consistent with values inferred from the fossils (29, 32) (*SI Text*). EM IV records times when the AIS margin retreated well inland and tundra occupied ice-free regions from the coast to at least 80 km inland (34)(Fig. 1 *C*, *v*).

Discussion

Proxy environmental data derived from AND-2A indicate coastal environments in SVL were highly variable throughout the early to mid-Miocene (Fig. 1 *B* and *C*). A robust age model for the AND-2A core (*Methods and Materials* and *SI Text*) allows us to integrate environmental data from the Antarctic coastal margin with regional seismic data from the Ross Sea continental shelf (35), deep sea oxygen and carbon isotope data (14, 15), sea level records (20), and atmospheric CO_2 reconstructions (3–9) (Fig. 2 and Fig. S5). We acknowledge that the age model for each dataset has uncertainties and caution that both proxy CO_2 reconstructions and sea level records are presently limited in temporal resolution and subject to large uncertainties. Despite these limitations, our correlation framework (Fig. 2 and Fig. S5) highlights several distinct episodes of (*i*) cold climate and marine-based ice sheet advance, (*ii*) peak warmth and maximum ice sheet retreat, and (*iii*) cold climate with relatively stable terrestrial ice sheets, which are discussed in detail below.

Four episodes of maximum ice sheet advance in the Ross Sea (MISA-1 to MISA-4) are documented between 21 and 13 Ma (Fig. 2 and Fig. S5). MISA episodes are recorded by stratigraphic gaps in AND-2A that correlate approximately in time with one of the major Ross Sea Unconformities (RSUs) that formed during ice sheet advance across the continental shelf (35). Each

MISA episode also correlates generally with an interval of global sea level fall, enrichment in deep-sea benthic $\delta^{18}O$, increase in benthic $\delta^{13}C$ values, and decrease in bottom water temperature (BWT) (Fig. 2 and Fig. S5). These patterns suggest episodes of maximum ice sheet advance were not restricted to the Ross Sea but represent continental scale expansion of the AIS. Importantly, our correlation model suggests that these MISA episodes coincided generally with eccentricity minima and intervals when atmospheric CO_2 concentrations were below 300 ppm (4, 5). MISA-3 (~14.6–14.7 Ma) best illustrates these associations (Fig. 2) and is characterized by an ~30-m drop in sea level (20), a 2–3 °C decrease in BWT in the Southern Ocean (17), a 0.75‰ enrichment in $\delta^{18}O$, a major increase in $\delta^{13}C$ (CM 5 from ref. 18) and a decrease in atmospheric CO_2 concentration to ~300 ppm (4, 5). MISA-4 (~13.7–14.1 Ma) (Fig. S5) coincides with the major Mi-3/E3 oxygen isotope excursion (16, 19), a drop in sea level of ~60 m (20), a 2–3 °C decrease in BWT (17), and a drop in CO_2 below 300 ppm (3, 5) (Fig. 2 and Fig. S5). MISA-3 and -4 correspond in time with RSU 4, a surface that displays erosional features with relief similar to bathymetric troughs that formed beneath ice streams during recent glaciations (36). RSU 4 likely formed during a phase of ice sheet advance and retreat that began ~14.6 Ma and culminated in the Miocene Climate Transition (MCT) and maximum ice sheet advance at 13.8 Ma. This phase of cold climate and persistent marine-based ice sheets ended at ~10 Ma when ice retreated to the terrestrial margins as revealed by upper Miocene mud-rich sediments in AND-1B (37).

Five episodes of peak warmth (PW-1 to PW-5), during which AIS grounding-lines retreated inland of the coastal margin, are also recorded. PW episodes are characterized by warm climate indicators in AND-2A (EM IV) that coincide generally with times of elevated BWT, depleted $\delta^{18}O$ values, eccentricity
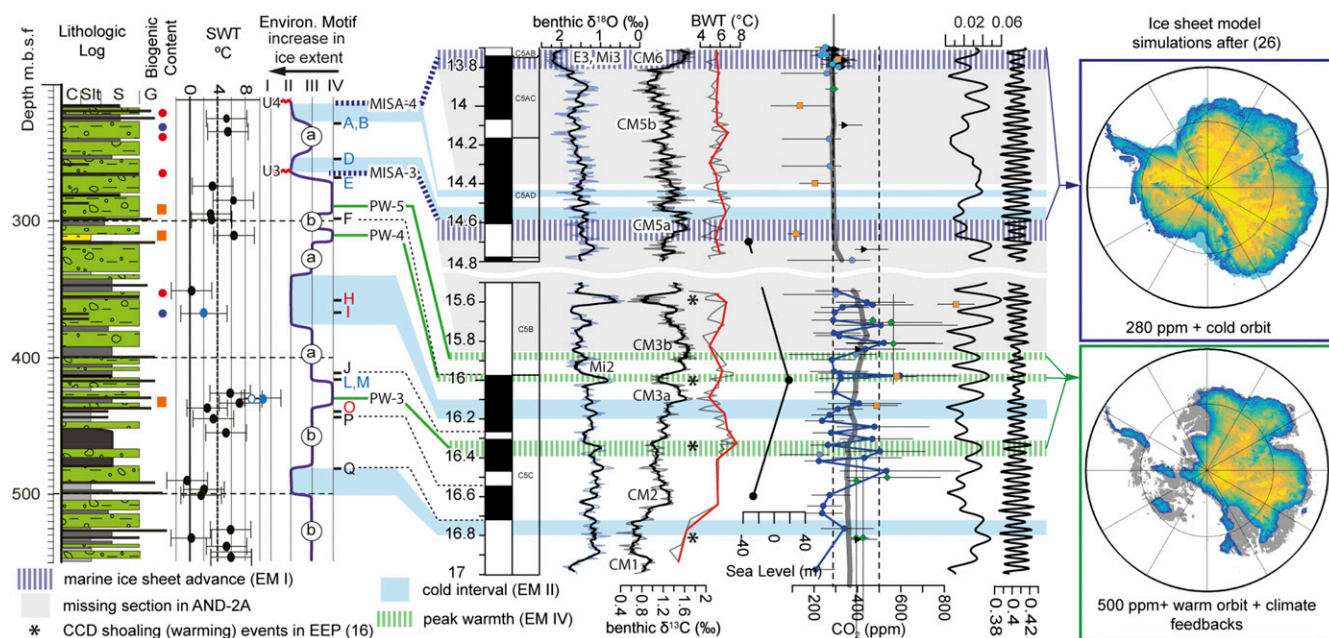

Fig. 2. Mid-Miocene section of AND-2A (557.35–214.13 mbsf) correlated to the Geomagnetic Polarity Timescale (46) and selected datasets. See Fig. 1 caption for description of AND-2A data. A–Q indicate position of key age model constraints (*SI Text*, Fig. S2, and Table S1). Benthic $\delta^{18}O$ and $\delta^{13}C$ isotope data with moving averages (thick lines) from IODP sites U1338 and U1337 (14, 15). Mi events after ref. 19 and E3 oxygen isotope excursion after ref. 16. CM, carbon isotope maxima (18, 39). Asterisks, carbon minima events and intervals of major shoaling of the carbonate compensation depth in the eastern equatorial Pacific (15). Bottom water temperature reconstructions from ref. 17 with 30-pt spline smooth (red line) (note: age model from ref. 17 adjusted by ~+50 ky for section between 15.5 and 17 Ma). Sea level data from the Marion Plateau (20). Proxy atmospheric CO_2 data include boron isotopes (3–5) (blue circles), alkenones (3, 6) (black triangles), stomata (7) (green diamonds), and paleosols (orange squares). Thick gray line = 21-point weighted average. Gray shaded boxes, time missing in unconformities; MISA (blue dashed line), maximum ice sheet advance (EMI); blue shaded zones, cold polar intervals (EMII); PW (green dashed line), peak warm intervals (EMIV). Orbital eccentricity and obliquity from ref. 48). Ice sheet simulations after ref. 25.

maxima, low $\delta^{13}C$ values, and relatively high atmospheric CO_2 concentrations (Fig. 2 and Fig. S5). Intervals PW-3, -4, and -5 occurred between 16.4 and 15.8 Ma (Fig. 2) and offer insight into AIS response during the MCO. Ice-distal sediments in these intervals are relatively rich in terrestrial palynomorphs, and proxies indicate that SWTs in the Ross Sea were 6–10 °C warmer than today. PW-4 (16 Ma) best illustrates these relationships as it correlates with a major (~0.5‰) decrease in $\delta^{18}O$, a 0.4‰ decrease in $\delta^{13}C$, a 2–3 °C increase in BWT at ODP site 1171 (17), and a 10- to 20-m rise in sea level across the Marion Plateau (20). Importantly, proxy data show that atmospheric CO_2 concentrations were >500 ppm during this warm episode (4, 7) (Fig. 2), which suggests that high latitude climate and Antarctica's terrestrial ice sheets were sensitive to CO_2 levels much lower than climate models suggest (38).

An unusual period of cold and relatively stable climate is suggested by proxies in the prominent thick interval of fine-grained sediments between 901.54 and 774.94 mbsf in AND-2A (sequence 18; Fig. 1B and Fig. S3). This unique stratigraphic interval is characterized by very low amounts of pollen and spores and persistently low SWTs (−1.3 °C to 2.6 °C). Foraminifera and diatoms are rare to absent. We infer the mudstone accumulated in a dark environment beneath semipermanent sea ice or an ice shelf. Interestingly, this interval correlates to upper Chron C6n, a time interval characterized by stable sea level (21) and low variability in orbital eccentricity (Fig. S5). Collectively, these data suggest that global climate and the AIS remained relatively stable through several glacial–interglacial cycles spanning at least 500 ky.

We conclude that environmental data from AND-2A and key far-field records indicate that Antarctica's climate and ice sheets were highly variable during the early to mid-Miocene. Whereas orbital variations were the primary driver of glacial cycles (28, 33, 39), atmospheric CO_2 variations modulated the extent of ice sheet advance and retreat. Specifically, coldest conditions and maximum ice sheet growth (MISA episodes and EM II) occurred generally during eccentricity minima and when atmospheric CO_2 was low (<400 ppm). Peak warmth and maximum AIS retreat occurred during eccentricity maxima and intervals of high CO_2 (≥500 ppm). Numerical climate and ice sheet model simulations produced in our companion study (25) (Fig. 2) support these observations and simulate grounding line advance across Antarctica's continental shelves under cold orbits and low CO_2 (280 ppm) but maximum retreat under warm orbital configuration and high CO_2 (500 ppm). Together, these studies suggest that polar climate and the AIS were highly sensitive to relatively small changes in atmospheric CO_2 during the early to mid-Miocene.

Summary

Our analysis of the AND-2A drill core and synthesis with regional and global data show that the early to mid-Miocene Antarctic coastal climate was highly variable. During relatively short-lived intervals of peak warmth, summer land surface air temperature was at least 10 °C, tundra vegetation extended to locations 80 km inland (34, 40), surface water temperatures in the Ross Sea were between 6 °C and 10 °C, and the AIS retreated inland. During intermittent intervals of peak cold climate, vegetation vanished

and the AIS grew and advanced into the marine environment, expanding across the continental shelf.

Whereas glacial cycles were paced by orbital variability through the early to mid-Miocene, maximum ice sheet retreat occurred when atmospheric CO_2 was ≥500 ppm and maximum advance when CO_2 was ≤280 ppm (Fig. 2 and Fig. S5) (4). New numerical ice sheet simulations (25) also show that the Miocene AIS expanded across the continental shelf when atmospheric CO_2 was low (280 ppm) and retreated well inland of the coast when CO_2 was high (500 ppm). These ice sheet proximal data and model simulations support inferences from benthic deep sea records that suggest the global climate system and AIS were highly sensitive during the mid-Miocene (14–16). These results are consistent with observations and numerical climate and ice sheet simulations based on the warm Pliocene (41–44), which indicate that sustained levels of atmospheric CO_2 >400 ppm may represent a stability threshold for marine-based portions of the West and East Antarctic ice sheets. Furthermore, outcomes from our complementary drill core analysis and ice sheet modeling indicate that Antarctica's terrestrial ice sheets were vulnerable when atmospheric CO_2 concentrations last exceeded 500 ppm. Given current atmospheric CO_2 levels have risen above 400 ppm (45) and are projected to go higher (2), paleoclimate reconstructions such as this one for the early to mid-Miocene imply an element of inevitability to future polar warming, Antarctic ice sheet retreat, and sea level rise.

Methods and Materials

Methods are presented in detail in *SI Text* and ref. 23. AND-2A was described using standard sedimentological techniques to produce detailed stratigraphic logs (27). An age model for the core (Fig. S2) uses magnetostratigraphy, biostratigraphy, $^{87}Sr/^{86}Sr$ dating of macrofossils, and ^{40}Ar-^{39}Ar ages on lava clasts and tephra layers to correlate rock units to the Global Polarity Timescale (46). Assemblages of fossil pollen, dinoflagellates, diatoms, foraminifera, and molluscs were used to constrain paleoenvironmental conditions. A standard suite of continuous physical properties was collected on whole and split core and in the borehole. Whole rock inorganic geochemical data were collected at high sampling resolution using an X-ray fluorescence core scanner (XRF-CS). Additional chemical data were collected from discrete bulk sediment samples at lower resolution to provide calibration points for near-continuous noninvasive sampling obtained via XRF-CS. Concentrations of Al_2O_3, Na_2O, CaO, K_2O, P_2O_5, and total organic carbon (TOC) from bulk sediment samples were used to calculate the CIA (47). Samples for TEX^L_{86} were prepared at Utrecht University and LC-MS analyses performed at the Royal Netherlands Institute for Sea Research. Samples for Δ_{47} (clumped isotopes) were prepared and analyzed at the California Institute of Technology.

1. IPCC (2013) *Climate Change 2013: The Physical Science Basis. Contribution of Working Group 1 to the Fifth Assessment Report Intergovernmental Panel on Climate Change* (Cambridge Univ Press, Cambridge, UK).
2. Meinshausen M, et al. (2011) The RCP greenhouse gas concentrations and their extensions from 1765 to 2300. *Clim Change* 109(1-2):213–241.
3. Badger MPS, et al. (2013) CO2 drawdown following the middle Miocene expansion of the Antarctic Ice Sheet. *Paleoceanography* 28(1):42–53.
4. Greenop R, Foster GL, Wilson PA, Lear CH (2014) Middle Miocene climate instability associated with high-amplitude CO2 variability. *Paleoceanography* 29(9):2014PA002653.
5. Foster GL, Lear CH, Rae JWB (2012) The evolution of pCO2, ice volume and climate during the middle Miocene. *Earth Planet Sci Lett* 341–344(0):243–254.
6. Zhang YG, Pagani M, Liu Z, Bohaty SM, DeConto R (2013) A 40-million-year history of atmospheric CO2. *Philo Trans R Soc A: Math Phys Engineer Sci* 371(2001):1–20.

7. Kürschner WM, Kvaček Z, Dilcher DL (2008) The impact of Miocene atmospheric carbon dioxide fluctuations on climate and the evolution of terrestrial ecosystems. *Proc Natl Acad Sci USA* 105(2):449–453.
8. Retallack GJ (2009) Greenhouse crises of the past 300 million years. *Geol Soc Am Bull* 121(9-10):1441–1455.
9. Ekart DD, Cerling TE, Montanez IP, Tabor NJ (1999) A 400 million year carbon isotope record of pedogenic carbonate: Implications for paleoatmospheric carbon dioxide. *Am J Sci* 299(10):805–827.
10. You Y, Huber M, Müller RD, Poulsen CJ, Ribbe J (2009) Simulation of the Middle Miocene Climate Optimum. *Geophys Res Lett* 36(4):1–5.
11. Herold N, Seton M, Müller RD, You Y, Huber M (2008) Middle Miocene tectonic boundary conditions for use in climate models. *Geochem Geophys Geosyst* 9(10): Q10009.

12. Herold N, Huber M, Müller RD (2011) Modeling the Miocene Climatic Optimum. Part I: Land and atmosphere*. *J Clim* 24(24):6353–6372.
13. Herold N, Huber M, Müller RD, Seton M (2012) Modeling the Miocene climatic optimum: Ocean circulation. *Paleoceanography* 27(1):PA1209.
14. Holbourn A, et al. (2014) Middle Miocene climate cooling linked to intensification of eastern equatorial Pacific upwelling. *Geology* 42(1):19–22.
15. Holbourn A, Kuhnt W, Kochhann KGD, Andersen N, Sebastian Meier KJ (2015) Global perturbation of the carbon cycle at the onset of the Miocene Climatic Optimum. *Geology* 43(2):123–126.
16. Flower BP, Kennett JP (1993) Middle Miocene ocean-climate transition; high-resolution oxygen and carbon isotopic records from Deep Sea Drilling Project Site 588A, Southwest Pacific. *Paleoceanography* 8(6):811–843.
17. Shevenell AE, Kennett JP, Lea DW (2008) Middle Miocene ice sheet dynamics, deep-sea temperatures, and carbon cycling: A Southern Ocean perspective. *Geochem Geophys Geosyst* 9(2):Q02006.
18. Woodruff F, Savin S (1991) Mid-Miocene isotope stratigraphy in the deep sea: High-resolution correlations, paleoclimatic cycles, and sediment preservation. *Paleoceanography* 6(6):755–806.
19. Miller KG, Wright JD, Fairbanks RG (1991) Unlocking the ice house: Oligocene-Miocene oxygen isotopes, eustasy, and margin erosion. *J Geophys Res* 96(B4):6829–6848.
20. John CM, et al. (2011) Timing and magnitude of Miocene eustasy derived from the mixed siliciclastic-carbonate stratigraphic record of the northeastern Australian margin. *Earth Planet Sci Lett* 304(3–4):455–467.
21. Kominz MA, et al. (2008) Late Cretaceous to Miocene sea-level estimates from the New Jersey and Delaware coastal plaoin coreholes: An error analysis. *Basin Res* 20:211–226.
22. Fretwell P, et al. (2013) Bedmap2: Improved ice bed, surface and thickness datasets for Antarctica. *The Cryosphere* 7(1):375–393.
23. Harwood D, Florindo F, Talarico F, Levy RH, eds (2008–2009) Studies from the ANDRILL Southern McMurdo Sound Project, Antarctica. Initial Science Report on AND-2A. *Terra Antarta* 15(1):235.
24. Fielding CR, Whittaker J, Henrys SA, Wilson TJ, Naish TR (2008) Seismic facies and stratigraphy of the Cenozoic succession in McMurdo Sound, Antarctica: Implications for tectonic, climatic and glacial history. *Palaeogeogr Palaeoclimatol Palaeoecol* 260(1):8–29.
25. Gasson E, DeConto R, Pollard D, Levy R (2016) A dynamic Antarctic Ice Sheet in the early to middle Miocene. *Proc Natl Acad Sci USA*, 10.1073/pnas.1516130113.
26. Passchier S, et al. (2011) Early and middle Miocene Antarctic glacial history from the sedimentary facies distribution in the AND-2A drill hole, Ross Sea, Antarctica. *Geol Soc Am Bull* 123(11-12):2352–2365.
27. Fielding CR, et al. (2011) Sequence stratigraphy of the ANDRILL AND-2A drillcore, Antarctica: A long-term, ice-proximal record of Early to Mid-Miocene climate, sea-level and glacial dynamism. *Palaeogeogr Palaeoclimatol Palaeoecol* 305(1-4):337–351.
28. Passchier S, Falk CJ, Florindo F (2013) Orbitally paced shifts in the particle size of Antarctic continental shelf sediments in response to ice dynamics during the Miocene climatic optimum. *Geosphere* 9(1):54–62.
29. Beu A, Taviani M (2013) Early Miocene Mollusca from McMurdo Sound, Antarctica (ANDRILL 2A drill core), with a review of Antarctic Oligocene and Neogene Pectinidae (Bivalvia). *Palaeontology* 57(2):299–342.
30. Patterson MO, Ishman SE (2012) Neogene benthic foraminiferal assemblages and paleoenvironmental record for McMurdo Sound, Antarctica. *Geosphere* 8(6):1331–1341.
31. Feakins SJ, Warny S, Lee J-E (2012) Hydrologic cycling over Antarctica during the middle Miocene warming. *Nat Geosci* 5(8):557–560.
32. Warny S, et al. (2009) Palynomorphs from a sediment core reveal a sudden remarkably warm Antarctica during the middle Miocene. *Geology* 37(10):955–958.
33. Griener KW, Warny S, Askin R, Acton G (2015) Early to middle Miocene vegetation history of Antarctica supports eccentricity-paced warming intervals during the Antarctic icehouse phase. *Global Planet Change* 127(0):67–78.
34. Lewis AR, Ashworth AC (2015) An early to middle Miocene record of ice-sheet and landscape evolution from the Friis Hills, Antarctica. *Geol Soc Am Bull*, 10.1130/B31319.1.
35. De Santis L, Anderson JB, Brancolini G, Zayatz I (1995) *Seismic Record of Late Oligocene Through Miocene Glaciation on the Central and Eastern Continental Shelf of the Ross Sea. Geology and Seismic Stratigraphy of the Antarctic Margin* (AGU, Washington, DC), Vol 68, pp 235–260.
36. Anderson JB, Bartek LR (1992) *Cenozoic Glacial History of the Ross Sea Revealed by Intermediate Resolution Seismic Reflection Data Combined with Drill Site Information. The Antarctic Paleoenvironment: A Perspective on Global Change*, eds Kennett JP, Warnke DA (American Geophysical Union, Washington, DC), Vol 56, pp 231–263.
37. McKay R, et al. (2009) The stratigraphic signature of the late Cenozoic Antarctic Ice Sheets in the Ross Embayment. *Geol Soc Am Bull* 121(11-12):1537–1561.
38. Goldner A, Herold N, Huber M (2014) The challenge of simulating the warmth of the mid-Miocene climatic optimum in CESM1. *Clim Past* 10(2):523–536.
39. Holbourn A, Kuhnt W, Schulz M, Erlenkeuser H (2005) Impacts of orbital forcing and atmospheric carbon dioxide on Miocene ice-sheet expansion. *Nature* 438(7067):483–487.
40. Lewis AR, et al. (2008) Mid-Miocene cooling and the extinction of tundra in continental Antarctica. *Proc Natl Acad Sci USA* 105(31):10676–10680.
41. Naish T, et al. (2009) Obliquity-paced Pliocene West Antarctic ice sheet oscillations. *Nature* 458(7236):322–328.
42. Cook CP, et al. (2013) Dynamic behaviour of the East Antarctic ice sheet during Pliocene warmth. *Nat Geosci* 6(9):765–769.
43. Pollard D, DeConto RM (2009) Modelling West Antarctic ice sheet growth and collapse through the past five million years. *Nature* 458(7236):329–332.
44. Pollard D, DeConto RM, Alley RB (2015) Potential Antarctic Ice Sheet retreat driven by hydrofracturing and ice cliff failure. *Earth Planet Sci Lett* 412(0):112–121.
45. Dlugokencky E, Tans P (2016) Trends in Atmospheric Carbon Dioxide. Available at www.esrl.noaa.gov/gmd/ccgg/trends/.
46. Ogg JG (2012) Geomagnetic polarity time scale. *The Geologic Time Scale*, eds Gradstein FM, Schmitz JGOD, Ogg GM (Elsevier, Boston), pp 85–113.
47. Nesbitt HW, Young GM (1982) Early Proterozoic climates and plate motions inferred from major element chemistry of lutites. *Nature* 299(5885):715–717.
48. Laskar J, Fienga A, Gastineau M, Manche H (2011) La2010: A new orbital solution for the long-term motion of the Earth. *Astron Astrophys* 532(A89):1–15.
49. Wilson DS, et al. (2012) Antarctic topography at the Eocene-Oligocene boundary. *Palaeogeogr Palaeoclimatol Palaeoecol* 335-336(2012):24–34.
50. Sugden D, Denton G (2004) Cenozoic landscape evolution of the Convoy Range to Mackay Glacier area, Transantarctic Mountains: Onshore to offshore synthesis. *Geol Soc Am Bull* 116(7-8):840–857.
51. Levy RH, et al. (2012) Late Neogene climate and glacial history of the Southern Victoria Land coast from integrated drill core, seismic and outcrop data. *Global Planet Change* 80-81(Special Issue):61–84.
52. Fitzgerald PG (1992) The Transantarctic Mountains of southern Victoria Land: The application of apatite fission track analysis to a rift shoulder uplift. *Tectonics* 11(3):634–662.
53. Kyle PR, Muncy HL (1989) Geology and geochronology of McMurdo Volcanic Group rocks in the vicinity of Lake Morning, McMurdo Sound, Antarctica. *Antarct Sci* 1(04):345–350.
54. Marcano MC, et al. (2009) Chronostratigraphic and paleoenvironmental constraints derived from the 87Sr/86Sr signal of Miocene bivalves, Southern McMurdo Sound, Antarctica. *Global Planet Change* 69(3):124–132.
55. Di Vincenzo G, Bracciali L, Del Carlo P, Panter K, Rocchi S (2009) 40Ar-39Ar dating of volcanogenic products from the AND-2A core (ANDRILL Southern McMurdo Sound Project, Antarctica): Correlations with the Erebus Volcanic Province and implications for the age model of the core. *Bull Volcanol* 72:487–505.
56. Florindo F, et al. (2013) Paleomagnetism and biostratigraphy of sediments from Southern Ocean ODP Site 744 (southern Kerguelen Plateau): Implications for early-to-middle Miocene climate in Antarctica. *Global Planetary Change* 110(0):434–454.
57. Talarico FM, Sandroni S (2011) Early Miocene basement clasts in ANDRILL AND-2A core and their implications for paleoenvironmental changes in the McMurdo Sound region (western Ross Sea, Antarctica). *Global Planet Change* 78(1–2):23–35.
58. Hauptvogel DW, Passchier S (2012) Early–Middle Miocene (17–14 Ma) Antarctic ice dynamics reconstructed from the heavy mineral provenance in the AND-2A drill core, Ross Sea, Antarctica. *Global Planet Change* 82–83:38–50.
59. Roser BP, Pyne AR (1989) Wholerock geochemistry. *Antarctic Cenozoic History from the CIROS-1 Drillhole, McMurdo Sound, DSIR Bulletin*, ed Barrett PJ (DSIR Publishing, Wellington, New Zealand), Vol 245, pp 175–184.
60. Bahlburg H, Dobrzinski N (2011) A review of the Chemical Index of Alteration (CIA) and its application to the study of Neoproterozoic glacial deposits and climate transitions. *Geol Soc Lond Mem* 36(1):81–92.
61. Schouten S, Hopmans EC, Schefuß E, Sinninghe_Damste JS (2002) Distributional variations in marine crenarchaeotal membrane lipids: A new tool for reconstructing ancient sea water temperatures. *Earth Planet Sci Lett* 204:265–274.
62. Kim J-H, et al. (2010) New indices and calibrations derived from the distribution of crenarchaeal isoprenoid tetraether lipids: Implications for past sea surface temperature reconstructions. *Geochim Cosmochim Acta* 74(16):4639–4654.
63. Kim J-H, et al. (2012) Holocene subsurface temperature variability in the eastern Antarctic continental margin. *Geophys Res Lett* 39(6):L06705.
64. Kalanetra KM, Bano N, Hollibaugh JT (2009) Ammonia-oxidizing Archaea in the Arctic Ocean and Antarctic coastal waters. *Environ Microbiol* 11(9):2434–2445.
65. Tierney JE, Tingley MP (2014) A Bayesian, spatially-varying calibration model for the TEX86 proxy. *Geochim Cosmochim Acta* 127:83–106.
66. Hopmans EC, et al. (2004) A novel proxy for terrestrial organic matter in sediments based on branched and isoprenoid tetraether lipids. *Earth Planet Sci Lett* 224(1–2):107–116.
67. Eagle RA, et al. (2013) The influence of temperature and seawater carbonate saturation state on 13C–18O bond ordering in bivalve mollusks. *Biogeosciences* 10(7):4591–4606.
68. Kim ST, O'Neil JR (1997) Equilibrium and non-equilibrium oxygen isotope effects in synthetic carbonates. *Geochim Cosmochim Acta* 61:3461–3475.
69. Marcano MC, Frank TD, Mukasa SB, Lohmann KC, Taviani M (2015) Diagenetic incorporation of Sr into aragonitic bivalve shells: Implications for chronostratigraphic and palaeoenvironmental interpretations. *The Depositional Record* 1(1):38–52.
70. Frank TD, Gui Z, ANDRILL SMS Science Team (2010) Cryogenic origin for brine in the subsurface of southern McMurdo Sound, Antarctica. *Geology* 38(7):587–590.
71. Liebrand D, et al. (2011) Antarctic ice sheet and oceanographic response to eccentricity forcing during the early Miocene. *Clim Past* 7(3):869–880.

Supporting Information

Levy et al. 10.1073/pnas.1516030113

SI Text

Miocene Paleogeography. Miocene paleogeography of the broader Ross Sea region is uncertain due to a relative paucity of geological data. However, reconstructions based on geodynamic modeling, backstripping, and erosion models indicate that much of West Antarctica was subaerial in the Eocene and early Oligocene (49), and, although subsidence history is unclear, seismic data suggest that structural ridges including the Coulman and Central highs formed relatively shallow marine ridges that were sites for ice cap growth during the late Oligocene-early Miocene. Geomorphologic data indicate the main outlet valleys dissecting the TAM were formed by rivers during the Eocene and were modified subsequently and/or incised via glacial processes under both temperate and polar climatic conditions (50). Exposed landforms and sediments preserved at high elevation are relict Miocene features that underwent little modification since middle Miocene time (50). Uplift has also been minimal since ~14 Ma, with rates of 100–200 m/My during the Late Neogene (51). A 15-Ma paleogeographic reconstruction for the Ross Sea region (Fig. S1) is based on a linear interpolation between reconstructed topography at the E/O boundary (49) and an isostatically rebounded version of modern topography (22).

Present-day geography in the vicinity of the AND-2A drillsite is dominated by the TAM to the west (Fig. S1), where mountain peaks in the Royal Society Range reach heights of >4,000 m. Uplift of this coastal mountain range began in the early Eocene (~55 Ma) at an average rate of 100 m/My and with subsequent removal (denudation) of 4.5–5 km of rock and sediment along the coastal wedge (52). Major Neogene alkalic volcanic features including Mount Discovery, Minna Bluff, Mount Morning, and Ross Island occur to the south and east of the drill site. This volcanic landscape is relatively young with most of these volcanic edifices postdating the AND-2A record. However, rock outcrop on Mount Morning have been dated at 18.7 and 14.6 Ma and indicate that volcanic features associated with the McMurdo Volcanic Group occurred in the region of the Koettlitz Glacier during the early to Middle Miocene (53).

Age Model. An age model for the core (Fig. S2) uses magnetostratigraphy (23), biostratigraphy (23), $^{87}Sr/^{86}Sr$ dating of macrofossils (54), and ^{40}Ar-^{39}Ar ages on volcanic clasts and tephra layers (55) to correlate rock units to the Global Polarity Timescale (46). Key events and tie points are summarized in Table S1. Biostratigraphic datums include first and last appearance of diatoms. The maximum and minimum age range reported for these datums are derived from the total, average, and hybrid range models of ref. 56, but we use the hybrid range model ages for tie points (marked by base of arrows in Fig. S2 and included in the text below).

The section from 1,138.54 (the base of AND-2A) to 986.94 mbsf is characterized by normal polarity (magnetozone N8). A radiometric date of 20.01 ± 0.12 Ma on pumice at 1,093 mbsf ties this normal interval to C6An.1n and the magnetic polarity reversal (MPR) at 986.94 mbsf to C6An.1n/C6r. Unconformity U1 occurs at the base of sedimentary cycle 14 and in the middle of magnetostratigraphic unit R7. We correlate the MPR at 958.59 mbsf (6.84 m above U1) to the C6r/C6n boundary based in part on radiometric dates of 19.61 ± 0.17 and 9.56 ± 0.12 Ma on pumice at 953.94 and 953.28 mbsf, respectively, that tie magnetozone N7 to C6n. This correlation suggests that ~200 ky is missing in U1. A radiometric age of 18.82 ± 0.15 Ma on pumice at 831.66 mbsf is consistent with our correlation of N7 with C6n and indicates that

the MPR at 783.69 mbsf is the C6n/C5Er boundary (18.748 Ma). U2 is located 8.75 m above the C6n/C5Er boundary at the base of cycle 22, which also contains the first occurrence (FO) of diatom *Thalassiosira praefraga* [first appearance datum (FAD): 18.58] and is characterized by a reversed polarity zone (R6). The last occurrence (LO) of *T. nansenii* (LAD: 17.5 Ma) at 763.84 mbsf indicates that sediments above this datum must be younger than ~17.5 Ma and suggests that the MPRs at 759.25 and 749.4 mbsf are correlated to C5Dr.1n/C5Dr.2r (17.74 Ma) and C5Dr.1r/C5Dr.1n (17.717 Ma) respectively. We note that this correlation requires that specimens of *T. praefraga* at 736.2 mbsf and pumice clasts at 709 mbsf have been reworked upcore. The diatom specimens occur in the middle of diamictite unit and pumice clasts occur in a sandstone unit. Reworking is certainly plausible. Furthermore, alternate solutions to the age model require downhole reworking of younger specimens, which is highly unlikely given the nature of this compact drill core. Therefore, we conclude the correlation presented herein is the most parsimonious.

We correlate the MPR at 722.45 mbsf with C5Dn/C5Dr.1r (17.533 Ma) based on the radiometric age of 17.5 ± 0.14 Ma on pumice from a tuff layer at 640.13 mbsf and infer that the dominantly normal magnetic stratigraphy between 722.45 and 581.34 mbsf correlates with C5Dn. Therefore, the MPR at 581.34 mbsf correlates with C5Cr/C5Dn (17.235 Ma). This solution is supported by the radiometric age of 17.2 ± 0.17 Ma on a lava clast at 564.92 mbsf and the occurrence of reversed magnetozones (R3.1 and R3.2) between 581.34 and 482.69 mbsf that likely correlate to the long reversed chron C5Cr (17.235–16.721 Ma). We infer that the C5Cn.3n/C5Cr boundary occurs at 482.69 mbsf but note that the boundary may lie anywhere between 482.69 and 460.62 mbsf as magnetostratigraphic measurements through this interval are ambiguous. The interval from 460.62 and 448.59 mbsf is characterized by normal polarity (magnetozone N3) and is correlated to C5Cn.3n. We tie the MPR at 448.59 to C5Cn.2r/C5Cn.3n (16.543 Ma). Reversed polarity interval R2.2 is tied to C5Cn.2r (16.472–16.543 Ma), and we correlate the ambiguous magnetozone from 439.23 to 429.56 with normal Chron C5Cn.2n (16.303–16.472 Ma) and reversed magnetozone R2.3 with C5Cn.1r. This solution is supported by the radiometric date of 16.64 ± 0.37 Ma on a lava clast at 440.83 mbsf and the FO of *Denticulopsis maccollumii* (FAD: 16.77 Ma) at 434.35 mbsf. This solution requires that the MPR at 412.71 mbsf correlates with C5Cn.1n/C5Cn.1r (16.268 Ma). We therefore infer that magnetozones N2.1A and B and N2.2 that occur between 412.71 and 328.52 mbsf, and the ambiguous magnetozones between the normal units, correlate with C5Cn.1n (15.974–16.268 Ma). This correlation is supported by strontium dates of 16.05 ± 0.35 Ma on an *Adamusium* shell fragment at 366.8 mbsf and radiometric date of 16.01 ± 0.17 Ma on a lava clast at 358.11 mbsf. Reversed polarity interval R2.0A and B must therefore correlate with C5Br but the exact location of the C5Cn.1n /C5Br boundary cannot be identified as the magnetic data are ambiguous. The absence of *Actinocyclus ingens* from the section below U2 suggests that the sediments immediately below the unconformity are at least older than 15.52 Ma (hybrid range model age for the FAD of *A. ingens*) and possibly older than 15.96 Ma (total range model age for the FAD of *A. ingens*). If we construct a line of correlation that accommodates all of the constraints outlined above, the C5Cn.1n/C5Br boundary would occur at the base of R2.0B.

Two major unconformities (U4 and U3) bracket the top 48.44 m of the section described in this paper. Rocks below the U4

disconformity contain the LO of diatom *Nitzschia* sp. 17 (230 mbsf, LAD: 14.94–13.7 Ma) and FO of *Actinocyclus ingens* var. *nodus* (237.03, FAD: 14.42–14.57 Ma), which indicate the sequence is at least older than 13.7 Ma. Magnetic polarity is uncertain through much of this section of AND-2A, although an interval of normal polarity occurs between 246.31 and 253.92 mbsf. We correlate this with C5ADn based on the FO of *A. ingens* var. *nodus*, which is located 9 m above the normal interval. We also infer that the slope of the LOC (sedimentation rate) for the sequence of rocks between U4 and U3 is similar to that defined immediately below U3. Therefore, the rocks most likely range in age from 14.6 to 14.4 Ma. U4 occurs between cycles 61 and 62 (214.13 mbsf). The absence of diatom taxa including *A. ingens* var. *nodus* (LAD: 12.57 Ma) and *Denticulopsis lauta* (LAD: 11.08 Ma) at 205 mbsf suggests that the overlying rocks are no older than 12.57 Ma and are possibly younger than 11.08 Ma. Radiometric ages of 11.363 ± 0.072 and 11.43 ± 0.46 Ma on crystals from reworked lava clasts at 127.50 and 129.96 mbsf, respectively, support this interpretation. Based on data described above, we infer the event(s) causing U4 must have occurred at or after 14.4 Ma (possible after 13.7 Ma based on LAD of *Nitzschia* sp. 17) and before 11 Ma.

Environmental Proxies and Interpretation. A summary of the suite of data and environmental proxies obtained from the AND-2A core is presented in Fig. S3. Details regarding these data and the environmental interpretations generated from the integrated proxy dataset are summarized below.

Sedimentology. Detailed sedimentological description and facies analysis provide the fundamental stratigraphic framework on which our paleoenvironmental interpretations are based. Nine nonvolcanic sedimentary facies are identified and range from diatomaceous siltstone to massive diamictite and matrix supported diamictite (26, 27), which reflect ice-distal to ice proximal (and occasional subglacial) settings, respectively. The Miocene lithologic succession is divided into sixty-one sequences on the basis of the repetitive vertical occurrence of characteristic facies that reflect cycles of advance and retreat of glaciers through the Transantarctic Mountains (27). Distinctive facies associations (26) and stratigraphic motifs (27) are distinguished based on diversity and abundance of different facies that reflect varying glacial environmental conditions.

Whereas details differ between climatic interpretations based on the facies association scheme (26) and stratigraphic motif designations (27), respectively, the long-term patterns of warming and cooling are compatible. Both interpretations suggest that diamictite-dominated sequences in the lowermost 250 m of the core (1,138.54–901.54 mbsf) reflect cold, subpolar, ice-proximal conditions. A 50-m-thick sequence of thin stratified diamictite and abundant mudstone (1,042.55–996.69 mbsf) in the middle of the diamictite-dominated interval indicates a period of ice-distal conditions and inferred warmer climate (27). A 100-m-thick mudstone dominated interval (901.54–774.94 mbsf) has been inferred to reflect deposition within a hemipelagic shelf environment with minimal glacial influence and a warmer temperate climate (26, 27). However, in this paper we argue that additional proxy climate data indicate that this interval reflects a cold climate and that the sediments were deposited beneath semi-permanent floating ice shelf or land-fast sea ice. An abrupt return to ice-proximal environments at the drill site is reflected in a 137-m-thick sequence (774.94–637.96 mbsf) that is dominated by massive and stratified diamictite. Passchier et al. (26) suggested that the facies associations between ~259 and ~648 mbsf are characteristic of open-shelf sedimentation under melt-water influenced settings and an inferred warmer climate. Stratified clast-rich diamictite units were deposited during glacial peaks and laminated and bioturbated mudstone intervals were deposited from sediment-rich plumes during interglacial periods. Massive and stratified diamictite dominated units above 259 mbsf

indicate a return to ice-proximal environments and colder climate. Fielding et al. (27) differ somewhat in their facies classification in this section of the core. They identified a lithologically diverse composite sequence and mudrock-dominated units from 637.96 to 389.03 mbsf and suggested that this sequence was deposited under a high-latitude temperate glacial regime. Diamictite-dominated units reflect a return to a subpolar glacial regime at 389.03 mbsf and a transition to cold subpolar/polar conditions at 296.34 mbsf. Regardless of the minor differences in composite unit boundaries, both lithologic interpretations imply that the sequence between 640 and 390 mbsf records an extended interval of diminished glacial influence at the drill site and that a transition to colder more ice-proximal environments occurs between 390 and 259 mbsf.

Most of the lithologic units in AND-2A contain gravel-sized clasts that were eroded from the TAM and transported to the drill site during advance of grounded ice and via melt-out from floating ice shelves and icebergs. The quantity and composition of clasts change in parallel with sedimentary facies and vary in abundance from their near absence (in cycles 9–12) to an interval with more than 1,000 clasts per meter. Changes in clast composition reflect the varying influence of different glacial drainages and have been used to infer periods of local vs. distal glacial sources (57). For example, the presence of foliated granodiorites and tonalities and medium-grade metamorphic rocks indicate provenance from basement rocks exposed in the Royal Society Range between the Blue and Koetlitz glaciers (57). In contrast, clast assemblages containing a distinctive monzogranite together with hornblende-biotite paragneiss and medium to high-grade metamorphic rocks are likely derived from rock exposure in the Britannia Range between the Carlyon and Byrd glaciers. Therefore, the distribution of distinctive basement clast assemblages in the AND-2A core reflect provenance from three regions including the Royal Society Range, the area between the Mulock and Skelton glaciers, and an area between the Carlyon and Darwin glaciers.

Changes in relative heavy mineral abundance delineate three intervals within the early to middle Miocene section of AND-2A (58). Interval I (Fig. S3) comprises three highly variable samples that are inferred to reflect provenance from rocks exposed at locations spanning the central TAM south of Byrd Glacier to the flanks of Mount Morning immediately south of the drill site. Of particular relevance is the high abundance of carbonate minerals in a sample at 599.02 mbsf, which suggests that glaciers were eroding limestone exposed at the coast of the central TAM. Interval II (Fig. S3) is dominated by heavy minerals derived from Ferrar Dolerite and high grade metamorphic rock exposures that suggest a local source in the vicinity of the Koettlitz Glacier. The presence of kyanite at several discrete horizons also suggests that ice periodically delivered sediment derived from rocks exposed in the Nimrod Glacier catchment. Increased abundance of heavy minerals with a Ferrar Group "fingerprint" indicates that glaciers had retreated from the coastal margin and were actively eroding dolerite sills exposed inland (58). Interval III (Fig. S3) is characterized by a decrease in the relative abundance of minerals derived from the Ferrar Group and high-grade metamorphic rocks, an increase in Granite Harbor intrusive rocks, and the reappearance of carbonate minerals. These data suggest that the EAIS margin readvanced, and outlet glaciers were actively eroding rocks exposed along the TAM front closer to the present-day coastline.

Paleontology. Whereas AND-2A is generally fossil poor, terrestrial flora and marine flora and fauna occur throughout the succession and are abundant in several discrete intervals (23). Assemblages of fossil foraminifera are dominated by calcareous benthic taxa. Intervals containing abundant and well-preserved forams extend to ~800 mbsf, and biogenic carbonate is present at several deeper horizons (30). Assemblages contain taxa that indicate paleo-water depths between 50 and 150 m (although depths up to 400 m are also possible). Notably, the interval above ~350 mbsf contains

the first occurrence of the cold water planktonic species *Neogloboquadrina pachyderma*.

Fossil diatoms generally occur in trace levels to the bottom of the core and are only abundant in four discrete intervals above 450 mbsf. The presence of *Paralia sulcata* between 430 and 434 mbsf indicates relatively shallow water depths (<100 m) at the drill site, which is consistent with foram data. *Thalassionema nitzschioides* is also recovered in this interval and indicates a cool water seasonally ice-free marine environment. A unique diatomite unit occurs between ~310 and 312 mbsf. This interval is dominated by *Chaetoceras* resting spores and contains the first occurrence of sea-ice indicators, including *Fragilariopsis truncata* and *Synedropsis cheethamii*, and taxa associated with ice-edge environments. *T. nitzschioides* also occurs in the diatomite unit, which indicates that seasonally ice free conditions existed at or nearby the drill site. Upcore diatom-rich intervals at 231–237 and 283–294 mbsf consist of massive, clast poor diamictite that was deposited in ice-proximal environments. Diatom assemblages recovered from these intervals are similar to those in the diatomite, although abundances are generally lower.

Marine palynomorph abundance and assemblage composition also fluctuates throughout the core (23). Many reworked Paleogene dinocyst specimens are present below ~857 mbsf. In situ dinocysts occur in discrete intervals throughout the core but specimens are most abundant above 430 mbsf. This *in-situ* dinocyst assemblage is dominated by *Operculodinim centrocarpum* and *Pyxidinopsis braboi* (32). High concentrations of these taxa occur within a diatom-bearing muddy diamictite at ~431 mbsf and peak concentrations occur in the diatomite at 312–310 mbsf. *Operculodinium centrocarpum* is an extant dinocyst that is distributed across a broad range of environments, but today it occurs in low abundance south of the Subantarctic Front. High numbers of both *O. centrocarpum* and *P. braboi* in these two distinct intervals in AND-2A indicate seasonally ice-free conditions (32).

Abundance and diversity of pollen and spores also vary throughout the core, although assemblage composition is relatively constant and comprises bryophyte spores, pteridophyte spores, and both conifer and angiosperm pollen. In general, the spore-pollen assemblages represent mossy tundra vegetation dominated by shrub podocarps and *Nothofagus* with a variety of subordinate plants dependent upon site microclimate and physiography (23, 32, 33). These data suggest that AND-2A records a general climate that was cooler than the modern austral polar-alpine tree limit in which the January mean temperature rarely exceeds 10 °C. However, an increase in *Podocarpites* pollen and peak counts of *Nothofagidites* pollen occur within the biosiliceous-bearing muddy diamictite between 432 and 434 mbsf and the diatomaceous mudstone between 312 and 310 mbsf and is concomitant with the increase in diatom and dinocyst abundance described above. This significant increase in terrestrial pollen may reflect an interval of elevated atmospheric temperature (>10 °C January mean), which allowed proliferation of woody plants (23) and possibly growth of tree-like forms (31). Increases in abundance of these pollen taxa also occur in discrete intervals within the lower sections of the core, although a comprehensive study through this interval has yet to be completed.

Finally, more than 600 marine macrofossil-bearing horizons occur throughout the core. Most of these fossil-bearing intervals are dominated by polychaete tubes but fragments of bryozoa, echinoderms, cirripeds, brachiopods, and a relatively diverse molluscan fauna are also present (23, 29). Well-preserved bivalves have been recovered from several discrete intervals and include an unusually diverse assemblage of six pectinid species that represent free-lying and attached forms. Of particular note is a "pectinid shellbed" at 430 mbsf, which contains the highest concentration of valves in the core (29). Most of the shells in this interval are crushed together at high angles, suggesting the de-

posit records a death assemblage that was likely transported from a shallow marine/subtidal environment and deposited in deeper water offshore. The unusually diverse pectinid assemblage reflects warmer temperatures in the Miocene than at present. Today, diverse large scallop assemblages are typically encountered in subpolar to temperate regions and do not occur further south than on the Magellanic shelf (57°S) and subantarctic waters around Campbell and Auckland Islands (55°S). Sea surface temperatures at these locations have an annual range between ~5 °C and 7 °C warmer than in the Ross Sea today (29).

Physical properties and inorganic geochemistry. A standard suite of continuous physical properties measurements were collected on whole and split core (23). Measurements of magnetic susceptibility reach their highest values (>200) within several relatively long intervals in the lower section of the core: 1,105–1,040, 990–950, and 850–775 mbsf. Shorter intervals occur from 990 to 980, 755 to 745, and 570 to 550, 480–470, and 445–435 mbsf. Most of the high susceptibility intervals generally correspond to units with high volcanic clast content. They also typically coincide with other proxy data that suggest cooler and drier climate including low CIA values and low TEX_{86}^L derived SWTs. These data suggest that intervals characterized by high magnetic susceptibility were deposited during episodes of concentrated glacial erosion of local volcanic rocks under cool/cold climatic conditions.

Whole rock inorganic geochemical data were collected from the AND-2A core at high sampling resolution using an XRF-CS (23). Additional data were collected from discrete bulk sediment samples at lower resolution (1–3 m) to provide calibration points for the near-continuous noninvasive samples obtained via XRF-CS. Percentage composition of major elements including TiO_2, Al_2O_3, CaO, K_2O, Fe_2O_3, Ce, Cr, Ni, Nb, and Zr were determined for the entire core. These data provide an additional tool to identify likely source rocks for glacial-marine sediments in the core, which can help constrain glacial reconstructions. For example, Niobium content is significantly higher in McMurdo Volcanic Group rocks (up to 200 ppm) (59) than in basement rocks exposed in the TAM. Therefore, intervals of high Nb content in the core reflect increased proportions of sediment derived from McMurdo Volcanic Group rocks exposed in the Mount Morning/Koetlitz Glacier region.

Inorganic geochemical data from bulk sediment samples has been used to calculate the CIA, which essentially provides a proxy for feldspar weathering but is generally used as a proxy for weathering of silicate rocks (47). The index is based on measured concentrations of Al_2O_3, Na_2O, CaO, and K_2O (on salt-free samples) and has been corrected for CaO associated with carbonate and phosphate minerals. Values <50 indicate that no, or only minimal, chemical weathering occurred, whereas CIA values >70 reflect significant chemical alteration (60). CIA values in AND-2A range between 46 and 68. CIA values determined from unweathered exposures of Ferrar Dolerite, McMurdo Volcanic Group, and Granite Harbor Intrusive Complex are typically around 50 or less. Therefore, intervals with low CIA values (<52) reflect a sediment source comprised of largely unweathered source rocks and likely indicate a cold and relatively dry climate with minimal time for source rocks to undergo chemical alteration. For instance, several intervals with low CIA values coincide with high magnetic susceptibility and high Nb XRF-CS counts. Together these data suggest that sediment was sourced from relatively unweathered McMurdo Volcanic Group rocks exposed in the region of Mount Morning. In contrast, the interval between ~400 and ~315 mbsf is characterized by low CIA values, magnetic susceptibility, and Nb concentration. These data indicate that sediment was derived from unweathered outcrop of Ferrar Dolerite and/or Granite Harbor Instrusives under cool and dry climatic conditions. Intervals with CIA values >60 are also typically associated with low magnetic susceptibility and Nb

concentration, which likely reflect sediment derived from more weathered outcrops of non-MVG rocks under warmer climate with more moisture available for silicate weathering.

Lipid biomarkers. Analyses of lipid biomarkers recovered from sedimentary sequences offer an ever-increasing range of proxy data for environmental reconstructions, which include sea surface water temperature (upper 200 m) (SWT), mean air temperature (MAT), and regional precipitation. Notably, proxies based on organic compounds have become a particularly important tool for high latitude reconstructions of SWTs through the Neogene as the sediments at these latitudes contain low amounts of carbonate material used in more traditional approaches. A lipid-based paleothermometer, TEX_{86} (61, 62), was applied to 49 samples in the AND-2A record to reconstruct SSTs (Fig. S3 and Table S3). We used the low temperature (0–200 m depth) calibration TEX_{86}^{L} (63), which is best suited for the polar oceans and Antarctic waters as it takes into consideration the depth in the water column where Thaumarchaeota (the organisms on which TEX_{86} paleothermometry is based) live year round (64).

Sea surface (upper 200 m) water temperature (SWT) is derived using the following equation:

$$SWT = 50.8 \times TEX_{86}^{L} + 36.1 \left(r^2 = 0.87; n = 396\right).$$

The calibration error is ±2.8 °C (62).

Results using an alternative calibration to that described in ref. 33 are also shown in Table S3. This calibration produces results with a similar trend but slightly different absolute temperatures. Furthermore, SWTs calculated using the Bayesian calibration of ref. 65 produce values that are several degrees higher, but the downcore trend remains similar (data not shown).

Samples with a branched vs. isoprenoid tetraether (BIT) index >0.3 (66) indicate high soil input and were not used to interpret SWTs. Samples with insufficient signal or poor peak resolution were discarded. We also consider the value of the sample at ~968 msbf unreliable as the sample occurs at an unconformity. Calculated SWTs vary throughout the early to middle Miocene section of the core and range from −1.4 to 7.0 ± 2.8 °C. Several intervals reveal persistent cold temperatures (SSTs <0 to ~2 °C), similar to those recorded in the Ross Sea today; these include an extended section from ~939 to ~700 mbsf. The warmest SST values between 6 °C and 7 °C occur in discrete intervals at 433, 311, and 285 mbsf. SSTs higher than 5 °C are rare below 500 mbsf and more common above this level.

A summary of TEX_{86}^{L} SWT data for EMs II, III, and IV is presented in Fig. S4 and highlights distinct differences between each motif.

Carbonate stable isotope ratios. The stable isotopic analysis of carbonates from sediments is widely used to constrain paleoenvironmental conditions. We measured carbonate $\delta^{18}O$, $\delta^{13}C$, and mass-47 (Δ_{47}) values in 37 samples of well-preserved to reasonably well-preserved carbonate macrofossils to determine SWT. Δ_{47} values form the basis for a new kind of stable isotope paleothermometer for carbonate minerals that is rooted in the same statistical thermodynamics as Urey's carbonate-water thermometer, but that circumvents the need to know the $\delta^{18}O$ of water.

Δ_{47} or "clumped" isotope thermometry is based on the principle that the pairing or clumping of heavy isotopes into bonds with each other in molecules is a temperature-dependent phenomenon. In carbonates, rare heavy isotopes (^{13}C, ^{18}O) occur in a pool of light abundant isotopes. Carbonate clumped isotope thermometry examines the proportion of ^{13}C and ^{18}O that are bound to each other within the carbonate mineral lattice. The extent of ordering is predicted to be temperature dependent based on theoretical calculations, with disorder increasing as temperature increases.

The basis for the clumping of these heavy isotopes into bonds with each other is thought to be the thermodynamically controlled exchange of stable isotopes among isotopologues of carbonate ion. The equilibrium constant for the reaction $^{12}C^{18}O^{16}O_2^{2-} + ^{13}C^{16}O_3^{2-} = ^{13}C^{18}O^{16}O_2^{2-} + ^{12}C^{16}O_3^{2-}$ forms the theoretical basis for carbonate clumped isotope thermometry, with the doubly substituted species (or heavy isotope clump) slightly more stable than the other isotopologues, and a progressively more random distribution of heavy isotopes among all possible isotopologues preferentially favored with increasing temperatures. So in an equilibrium precipitate, if the equilibrium constant for the above reaction is known and the abundance of all four isotopic species is measured, the temperature can be calculated independent of the isotopic composition of the water in which the carbonate grew. In addition, clumped isotope-derived temperatures can be combined with carbonate $\delta^{18}O$ to estimate water $\delta^{18}O$, by applying an appropriate carbonate-water oxygen-isotope fractionation relationship.

In practice, carbonate clumped isotope thermometry is based on analyses of $^{13}C^{18}O^{16}O$ in CO_2 (which has a mass of 47 amu) that is produced by acid digestion of $CaCO_3$. Fractionation during acid digestion is ~0.2 per mil (‰) and is a predictable function of acid-digestion temperature. The abundance of the doubly substituted isotopologue $^{13}C^{18}O^{16}O$ is reported using the variable Δ_{47}. Δ_{47} is defined as the ‰ enrichment of $^{13}C^{18}O^{16}O$ above the amount expected for a random distribution of isotopes.

The methods and instrumentation used are identical to those used in a previous study (67). Briefly, samples were digested at Caltech at either 25 °C in a two-legged reaction vessel or on a 90 °C common acid bath system with automated cryogenic and chromatographic purification. An acid digestion fractionation factor of 0.092‰ was used to correct 90 °C-reacted samples to 25 °C. Measurements were made on a Finnegan MAT 253 gas source mass spectrometer at Caltech with 1 SE precision as good as ±0.009‰. The total analysis time (including peak centering, background measurement, and pressure balancing) ranged from 4 and 8 h. Measurements were made to yield a 16-V signal for mass 44, with peak centering, background measurement, and pressure balancing before each acquisition. These conditions were selected to ensure stable ion currents and minimize time-dependent fractionation of sample and reference gas reservoirs.

Each day we analyzed a heated gas composed of CO_2 with a stochastic distribution of isotopes between isotopologues. Gases with different bulk $\delta^{18}O$ and $\delta^{13}C$ ratios in quartz breakseals were heated to 1,000 °C for 2 h and then quenched at room temperature. These standard gases (or heated gases) were then purified and analyzed using the same protocol as sample gases. Our analysis were conducted before the proposition of a new reference frame for Δ_{47} measurements based on normalization to a reference gas equilibrated with water, and therefore samples were projected onto the absolute reference frame using carbonate standard data.

Temperatures were calculated using a new mollusk calibration equation (67), which was generated using the same methods and instrumentation described herein. For calculations of equilibrium $^{18}O/^{16}O$ ratios in calcite (and to calculate $\delta^{18}O$-calcification temperatures), we used a published relationship from Kim and O'Neil (68) to describe calcite-water fractionation. This calibration line is used in this study as it spans a temperature range (−1 to 30 °C) appropriate for work on the Antarctic and includes measurements from modern specimens collected in shallow Southern Ocean sites including the Ross Sea and Ushuaia. This calibration was also generated using the same 90 °C common acid bath digestion and automated sample cleanup apparatus and mass spectrometer systems that were used to make measurements on the ANDRILL samples.

Well-preserved specimens were identified based on visual appearance and previously published Sr isotope data and

elemental ratios (54, 69). In addition, we measured other samples that were visibly well preserved and yielded plausible seawater $\delta^{18}O$ values (i.e., nonbrine water $\delta^{18}O$) (70). These samples were classified as possibly well preserved. Reconstructed water $\delta^{18}O$ values for all samples range from 0‰ to 2‰ (Table S4). Miocene Δ_{47}-SWT estimates (Table S4) are similar to those based on paleoecology and TEX$_{86}$ paleothermometry and match published model results (31).

Fig. S1. (*Top Left*) Ross Sea regional topography (ice sheet removed). Red square indicates area of sketch at right, which shows major geographic and topographic features in the region of the AND-2A drill hole (dashed lines indicate Late Neogene volcanic features). (*Bottom Left*) Miocene topography is based on a linear interpolation between an Eocene/Oligocene reconstruction (49) and an isostatically rebounded version of BEDMAP-2 (22). Sketch at right shows reconstruction of early Miocene topography in the region of the drill site.

Fig. S2. Age-depth model for AND-2A.

Fig. S3. Stratigraphic and chronologic summary of the lower 925 m of the AND-2A core showing 61 sedimentary cycles of ice sheet margin advance, retreat and readvance before, during, and immediately following the MCO. Lithologies (rock types) are plotted against depth; s, shear fabric and inferred glacial overriding. Facies associations are after ref. 26 and stratigraphic motifs and sequences are defined by ref. 2. A glacial proximity curve tracks the relative position of the grounding line through ice-contact (I), ice-marginal (IM), ice-proximal (P), ice-distal (D), and open marine (O) environments. Heavy mineral assemblage intervals (I–III) are from ref. 58, and green circles indicate horizons with kyanite likely derived from the Nimrod Glacier catchment. Clast provenance indicates the relative influence of ice flowing from the Royal Society Range west/southwest of the drill site (red), the Skelton and Mulock glacier catchments (yellow), and Carlyon and Byrd glacier catchments (orange). Clast abundance is plotted in 1-m interval bins. Foram abundance data from ref. 30. Inferred cold water/ice marginal assemblages (*Ehrenbergina*) are indicated by red circles and occurrences of cool water planktonic species by green (*Globorotalia* spp.) and blue (*Neogloboquadrina pachyderma*) circles. Diatom abundance data after ref. 23. Blue bars indicate presence of sea ice species. Palynomorph data include in situ dinocyst and *Nothafagidites* counts per gram of dry sediment down to 650 mbsf (32) and whole counts of Podocarpacea to the base of the core. Intervals containing well-preserved molluscs reported in ref. 29 are indicated with an M. Organic lipid biomarkers include TEX$_{86}$ from Thaumarcheota. Low temperature TEX$_{86}^{L}$ calibration (63) was used to calculate SWT estimates (red line). CIA provides an indication of arid (<52, blue) and less arid (>58, green) conditions.

Fig. S4. Box and whisker plot showing TEX_{86}^L sea water temperature data for environmental motifs II, III, and IV.

Fig. S5. Integrated environmental dataset through the early to middle Miocene correlated to the Geomagnetic Polarity Timescale (46). Stra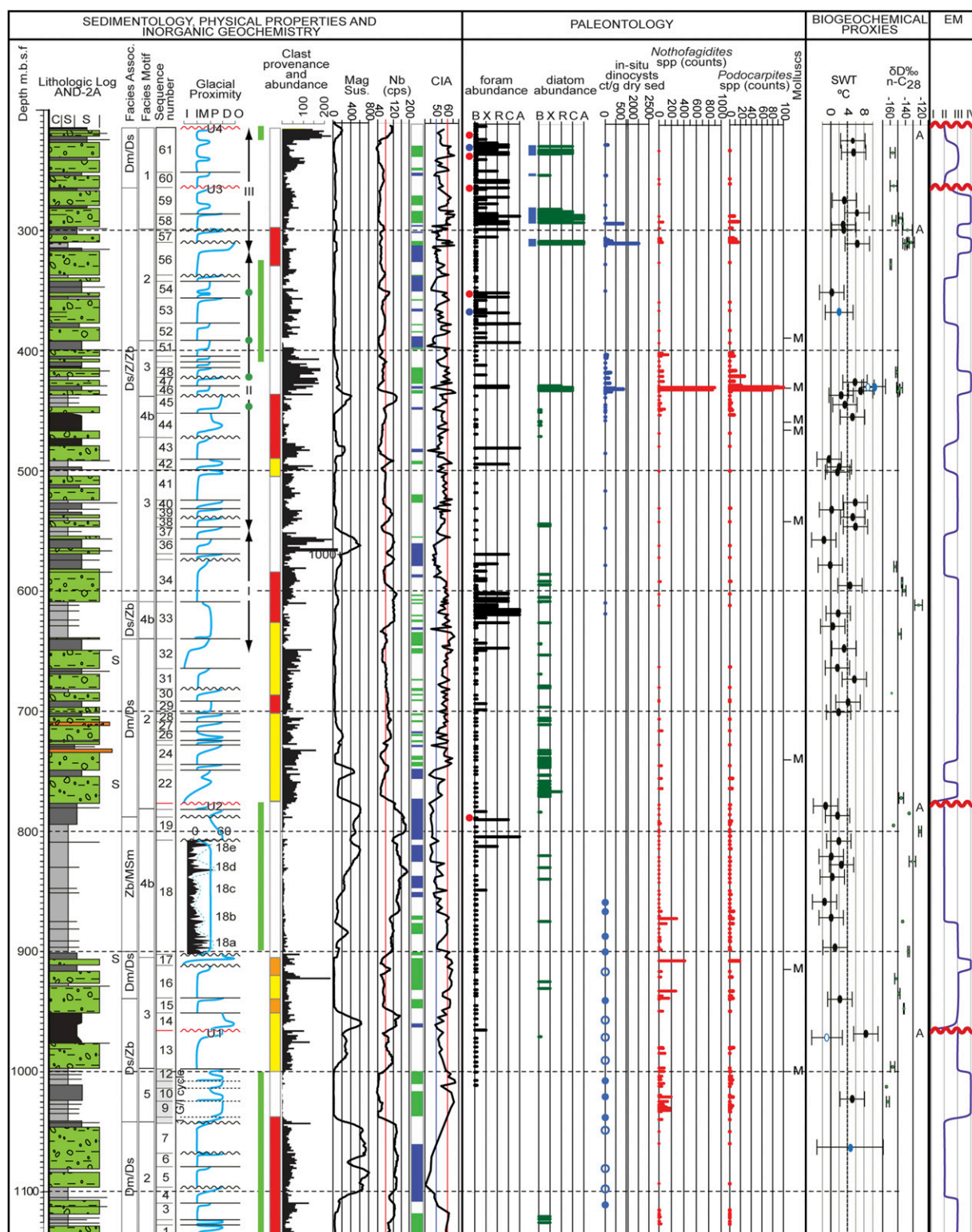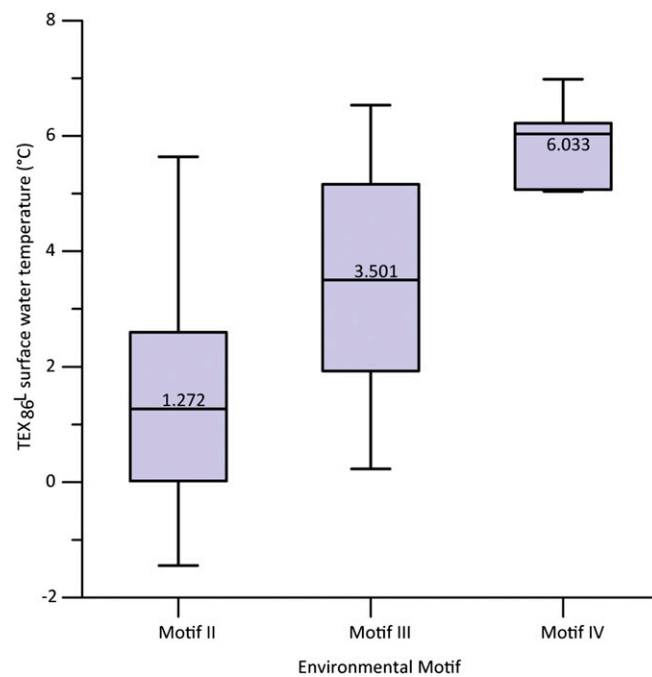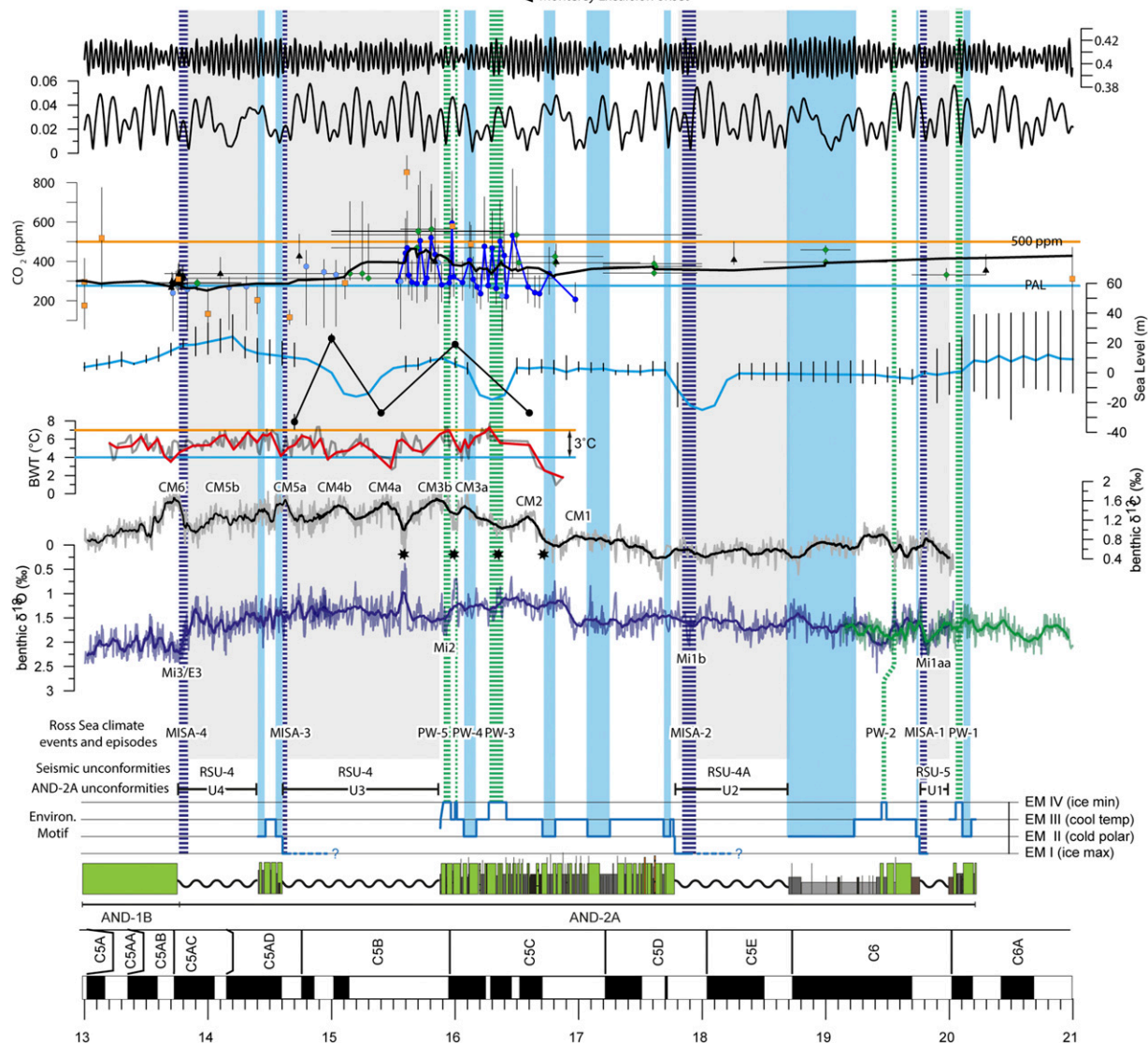tigraphic column includes data from AND-2A and lowermost portion of AND-1B. Blue curve shows environmental motif (I–IV) interpreted from AND-2A. Chronostratigraphic position of major disconformities in AND-2A and equivalent Ross Sea seismic unconformities (RSUs) (35) indicated by black bars. Benthic δ18O and δ13C isotope data with moving averages (thick lines) from IODP sites U1338 and U1337 (blue) (14, 15) and from ODP site 1264 (green) (71). Mi events after ref. 19 and E3 oxygen isotope excursion after ref. 16. CM, carbon isotope maxima (18, 39); asterisks, carbon minima events and intervals of major shoaling of the carbonate compensation depth in the eastern equatorial Pacific (15). Bottom water temperature reconstructions from ref. 17 with 30-pt spline smooth (red line). Sea level data from the Marion Plateau (black) (20) and New Jersey Margin (blue) (21). Proxy atmospheric CO_2 data include boron isotopes (3–5) (blue circles), alkenones (3, 6) (black triangles), stomata (7) (green diamonds), and paleosols (orange squares). Thick gray line, 21-point weighted average; gray shaded regions, time missing in unconformities; MISA (blue dashed line), maximum marine ice sheet advance; blue shaded zones, cold polar intervals (EMII); PW (green dashed line), peak warm intervals. Orbital eccentricity and obliquity from ref. 48.

Table S1. Chronostratigraphic data used to establish the age model for AND-2A presented in this paper (Fig. S1)

Depth	Event	Description	Type	Age (Ma)	Ref.
214.13	U-4	Base cycle 62	Unconformity	~14.4–~9.7 (up to 4.7 My missing)	
230.25	A	*Nitzschia* sp. 17	LAD	13.7–14.94	(56)
237.03	B	*Actinocyclus ingens* var. *nodus*	FAD	14.42–14.57	(56)
253.92	C	Lower C5ADn	Normal polarity	<14.581	(46)
255.2	D	*Actinocyclus ingens*	FAD	15.05–15.96	(56)
262.57	U-3	Base cycle 60	Unconformity	15.8–14.6 (~1.2 My missing)	
263	E	Absence of *A. ingens*	FAD	>15.96	(56)
298.34	F	C5Br/C5Cn.1n (?)	MPR	15.974	(46)
328.52	G	C5Cn.1n	Normal polarity	>15.974	(46)
358.11	H	Lava clast (Diamictite)	$^{40}Ar/^{39}Ar$ date	15.91 ± 0.29	(55)
366.8	I	*Adamusium* shell	$^{87}Sr/^{86}Sr$ date	16.05 ± 0.35	(54)
412.71	J	C5Cn.1n/C5Cn.1r	MPR	16.268	(46)
429.56	K	C5Cn.1r/C5Cn.2n (?)	MPR	16.303	(46)
434.35	L	*Denticulopsis maccollumii*	FAD	16.23–17.03	(56)
434.35	M	*Nitschia* sp. 17	FAD	16.77–17.94	(56)
439.23	N	C5Cn.2n/C5Cn.2r (?)	MPR	16.472	(46)
440.83	O	Lava clast (Mudstone)	$^{40}Ar/^{39}Ar$ date	16.54 ± 0.43	(55)
448.59	P	C5Cn.2r/C5Cn.3n	MPR	16.543	(46)
482.69	Q	C5Cn.3n/C5Cr (?)	MPR	16.721	(46)
564.92	R	Lava clast (Conglomerate)	$^{40}Ar/^{39}Ar$ date	17.1 ± 0.31	(55)
581.34	S	C5Cr/C5Dn	MPR	17.235	(46)
640.13	T	Pumice (Lapilli tuff)	$^{40}Ar/^{39}Ar$ date	17.5 ± 0.14	(55)
709.14	U	Pumice (Tuffaceous sst)	$^{40}Ar/^{39}Ar$ date	18.26 ± 0.21	(55)
709.17	V	Pumice (Tuffaceous sst)	$^{40}Ar/^{39}Ar$ date	18.04 ± 0.31	(55)
722.45	W	C5Dn/C5Dr.1r	MPR	17.533	(46)
736.2	X	*Thalassiosira praefraga*	LAD	17.94–17.95	(56)
749.4	Y	C5Dr.1r/C5Dr.1n	MPR	17.717	(46)
759.25	Z	C5Dr.1n/C5Dr.2r	MPR	17.74	(46)
763.84	AA	*Thalassiosira nansenii*	LAD	17.5	
771.5	AB	*Thalassiosira praefraga*	FAD	18.46–18.58	(56)
774.94	U-2	Base cycle 22	Unconformity	18.7–17.8 (~900 ky missing)	
783.69	AC	C5Er/C6n	MPR	18.748	(46)
831.66	AD	Pumice (Tuffaceous zst)	$^{40}Ar/^{39}Ar$ date	18.82 ± 0.15	(55)
953.28	AE	Pumice (Tuffaceous sst)	$^{40}Ar/^{39}Ar$ date	19.56 ± 0.12	(55)
953.94	AF	Pumice (Tuffaceous sst)	$^{40}Ar/^{39}Ar$ date	19.61 ± 0.17	(55)
958.59	AG	C6n/C6r	MPR	19.722	(46)
965.43	U-1	Base of cycle 14	Unconformity	20–19.8 (~200 ky missing)	
986.94	AH	C6r/C6An.1n	MPR	20.04	(46)
1,093	AI	Pumice (Tuffaceous sst)	$^{40}Ar/^{39}Ar$ date	20.13 ± 0.15	(55)
1,138.54	AJ	C6An.1n	normal polarity	<20.213	(46)

Table S2.   Summary of proxy data used to define environmental motifs for AND-2A

Environmental motif	Lithofacies	Provenance	Weathering index (CIA)	Biofacies	Proxy SWT (TEX$_{86}$ and Δ_{47}) range (°C)	Climate and glacial regime
EMI	Significant time break (major erosion surface in core)	NA	NA	NA	NA	Cold polar conditions with ice sheets that advanced well into the marine environment
EMII	Dominated by massive and stratified diamictite and bioturbated siltstone.	High magnetic susceptibility, high Nb (volcanic signature), gravel derived from Koetlitz Glacier and Royal Society Range.	Low	Very rare fossil component	−1.4 to 2.6	Cold polar conditions with minimum marine-based grounding-line variability and persistent floating ice shelves and/or land-fast sea ice along the coast.
EMIIIa	Dominated by stratified diamictite and gravel with abundant stratified sandstone.	Low magnetic susceptibility with low to moderate Nb, gravel source is typically mixed but includes clasts derived from the region between Mulock and Skelton glaciers.	Moderate to high	Rare to common fossil content	2.2–5.4	Subpolar conditions with tidewater glaciers that calved at the coast.
EMIIIb	Dominated by stratified diamictite and gravel with common sandstone and siltstone.	Low magnetic susceptibility with low Nb, gravel source is typically mixed but includes clasts derived from the region between Carlyon and Darwin glaciers.	Moderate to high	Palynomorphs rare to abundant, abundant molluscs	0.2–6.7	Subpolar conditions with tidewater glaciers that calved at the coast and periodically retreated onto land. Includes intervals when small regions of tundra spread along the coast.
EMIV	Dominated by stratified mudstone with common gravel and stratified diamictite.	Low magnetic susceptibility with low Nb.	High	Diatoms, palynomorphs, foraminifera, and molluscs abundant	3.0–10.4	Subpolar to cool temperate maritime climate along the coast. Glaciers grounded on land. Tundra growing from the coast to at least 80 km inland.

NA, not applicable.

Table S3.   Organic lipid data from AND-2A

Core depth (mbsf)	BIT index	SWT °C (0–200 mbsf) calibration after ref. 63	Core depth (mbsf)	BIT index	SWT °C (0–200 mbsf) calibration after ref. 63
142.90	0.25	4.0	578.49	0.04	0.0
198.41	0.08	4.2	595.50	0.07	4.6
225.42	0.20	5.2	618.56	0.05	1.8
235.11	0.11	5.4	629.38	0.03	0.6
274.92	0.08	3.3	647.64	0.12	3.2
285.35	0.11	6.1	663.69	0.15	1.7
295.25	0.07	3.0	673.17	0.18	5.5
299.42	0.18	3.1	692.24	0.09	4.1
311.07	0.09	6.2	700.49	0.17	1.9
336.13	0.32	3.2	727.68	0.09	6.5
351.59	0.03	0.4	778.50	0.14	−1.0
426.29	0.17	5.7	786.52	0.16	1.7
433.49	0.14	7.0	807.76	0.07	2.0
437.20	0.25	2.5	820.60	0.25	0.3
445.07	0.23	3.4	827.51	0.06	2.6
455.27	0.29	5.1	837.64	0.08	0.5
463.26	0.33	6.7	858.37	0.05	−1.3
490.26	0.16	−0.2	871.50	0.05	0.2
496.76	0.13	2.1	896.27	0.06	1.1
501.02	0.25	1.7	939.35	0.14	2.2
526.28	0.12	5.8	968.15	0.10	8.2
532.41	0.10	0.3	987.33	0.08	7.0
538.56	0.09	5.2	1,022.36	0.07	5.1
546.49	0.26	5.8	1,125.97	0.10	2.6
557.54	0.29	−1.4			

Table S4. Stable isotope data

Core depth (mbsf)	No. of analyses	Sample ID	Type	$d^{13}C$ (‰, V-PDB)	SD	$d^{18}O$ (‰, V-PDB)	SD	D_{47} (‰, ARF, AFF-corrected)	SE	D_{47}-T	SE	Water $d^{18}O$ (‰, V-SMOW)	SE
366.8	**1**	**AND-2A 366.80 (MM-7)**	**Bivalve**	**4.04**	**0.01**	**2.17**	**0.01**	**0.792**	**0.013**	**2.1**	**3.7**	**−0.5**	**0.9**
430.49	**1**	**AND-2A 430.49–430.51 (MM-10)**	**Veneridae**	**1.16**	**0.00**	**−0.38**	**0.01**	**0.764**	**0.008**	**10.4**	**2.5**	**−1.9**	**0.5**
430.54	2	AND-2A 430.54–430.68 (11)	Bivalve	3.66	0.00	0.82	0.02	0.758	0.004	12.3	1.3	0.5	0.3
430.54	4	AND-2A 430.54 430.68 frag a	Bivalve	3.46	0.02	0.70	0.27	0.793	0.012	1.7	3.5	−2.0	0.8
430.54	5	AND-2A 430.54 430.68 frag b	Bivalve	2.81	0.11	−0.44	0.49	0.765	0.015	10.2	4.7	−1.2	1.1
430.54	5	AND-2A 430.54 430.68 frag c	Bivalve	2.67	0.10	−0.63	0.30	0.759	0.009	12.0	3.0	−1.0	0.7
450.54	3	AND-2A mm 11–1 25 °C (450.54–430.68 - inner layer)	Costate Pectinid	2.32	0.10	−1.46	0.54	0.771	0.006	8.3	1.8	−2.6	0.5
450.54	2	MM-11–2 (450.54–430.68 - outer ribbed layer)	Costate Pectinid	1.92	0.22	−2.05	0.44	0.772	0.026	8.1	7.9	−3.3	1.8
970.74	4	AND2-2A 970.74–970.83 (25 °C)	Bivalve	2.68	0.40	1.68	0.11	0.802	0.014	−0.8	3.9	−1.7	0.9
1063.71	**2**	**AND2-2A 1063.71–1063.75 (25 °C)**	**Adamussium alanbeui**	**3.81**	**0.01**	**1.16**	**0.11**	**0.783**	**0.027**	**4.7**	**2.4**	**−0.9**	**0.6**

Bold indicates well-preserved specimens. Less well-preserved material in plain text.

Other Supporting Information Files

SI Appendix (DOC)